Journal of Applied Fluid Mechanics, Vol. 17, No. 6, pp. 1182-1190, 2024.
Available online at www.jafmonline.net, ISSN 1735-3572, EISSN 1735-3645.
https://doi.org/10.47176/jafm.17.6.2403

Aerodynamic Performance of Lambda Wing-UCAV at Different Back-sweep Angles

S. Syam Narayanan†, Y. Gangurde and P. Rajalakshmi

NMICPS Technology Innovation Hub on Autonomous Navigation, Indian Institute of Technology, Hyderabad, India

†*Corresponding Author Email: ee22pdf06@iith.ac.in*

ABSTRACT

Unmanned Combat Aerial Vehicles (UCAVs) are designed to be lightweight and compact, which can impact their overall lift and aerodynamic capabilities. This study focuses on enhancing the Coefficient of Lift (C_L) by optimising the Back Sweep Angle in the Lambda wing-UCAV. The model's baseline geometry remains unchanged during the experimental and numerical analysis, while different back sweep angles ranging from $\delta=0^0$ to $\delta=50^0$ are investigated at varied free-stream velocities and angles of attack. This helps to understand the generation of induced lift in the intricate shapes of the Lambda Wing. The results indicate a 5% to 10% increase in the lift for every 10^0 increments of the Back Sweep Angle, and the vortices' strength increases and reaches a maximum at $\delta=40^0$. At greater angles ($\delta > 40^0$), the lift drops gradually with the Reynolds number. The stagnation point shifts from 25% to 35% along the chord towards the pressure surface as the angles of attack increase from $\alpha=5^0$ to $\alpha=10^0$. The angle of attack $\alpha>10^0$.

Article History

Received October 28, 2023
Revised December 30, 2023
Accepted January 16, 2024
Available online March 27, 2024

Keywords:

Computational Fluid Dynamics
Lambda Wing
Back Sweep Angle
Unsteady Vortices
UCAV

1. INTRODUCTION

An Unmanned Combat Aerial Vehicle (UCAV), also known as a battlefield UAV, represents a distinct category within Unmanned Aerial Vehicles (UAVs). The primary role of UCAVs is targeted attacks, involving the transportation and deployment of armaments such as missiles or explosives. Other applications include reconnaissance, target identification, and surveillance activities to gain valuable intelligence (Narayanan & Ahmed, 2021). These UAVs often have varying degrees of autonomy, which human operators control in real-time. Unlike UAVs, which can serve various functions, designers build UCAVs from the ground up to conduct drone assaults and gather battlefield data (S. & R., 2022). This vehicle operates by a remote control terminal, making it lighter and more compact than a conventional aeroplane (Lakshmanan et al., 2023). The number of countries operating Unmanned Combat Aerial Vehicles (UCAVs) is growing, and many more are importing armed drones or working to create their own (Coppin et al., 2018).

Compared with standard Unmanned Aerial Vehicles, the wing carries fuel, equipment, and engines in this configuration. Hence, the plane maintains its basic triangle or lambda shape. The wing construction is delta (triangular) and stands independently without a fuselage (Cummings & Schütte, 2012).

Lambda wings are delta wings with a modification to the trailing edge in the form of a crank connecting two 'V-shaped patterns (Chaplin & Birch, 2012). The term "lambda wing" comes from the shape of the trailing edge crank, which resembles the Greek letter "lambda" in lowercase (Fig.1). When the flow is forward, the strongest

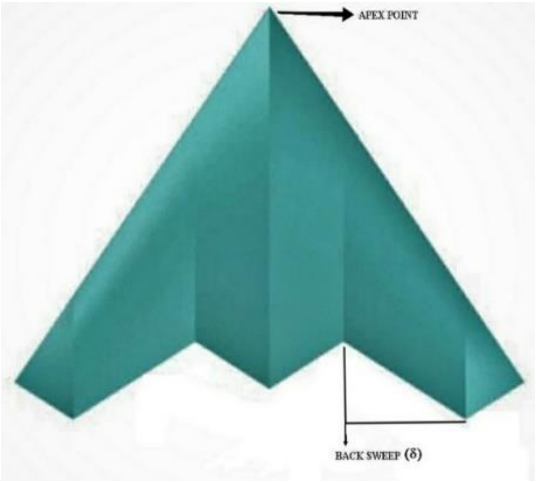

Fig. 1 Lambda wing

NOMENCLATURE

c	mean aerodynamic chord	S	span area
C_D	coefficient of drag	V_∞	free stream velocity of air
C_L	coefficient of lift	α	angles of attack
D	drag force	δ	back sweep angle
L	lift force	μ	dynamic viscosity of air
Re	Reynold's number	ρ	density of air

In recent years, research has been conducted on lambda and delta wings for application on Unmanned Combat Aerial Vehicles (UCAV) to meet in-flight requirements and increase the performance and aerodynamic characteristics of wings used for UCAVs operating at subsonic and supersonic speeds. As a result of the optimisation technique between subsonic and supersonic speeds, a wing designed for optimal performance in a one-speed regime must endure a high drag cost in another (Younis et al., 2012).

Issues with engine integration, control, and stability, as well as the drag penalty associated with subsonic and supersonic speed during the take-off, climb, descent, and landing phases of a UCAV (Al-Garni et al., 2008) are buffet is between the leading-edge vortex system's primary attachment and the vortex core (Frink et al., 2012).

encountered. Therefore, researchers have conducted extensive experimental, numerical, and atmospheric flight conditions testing and computational fluid analysis to meet mission requirements and adapt the UCAV to its operating environment (Nagel et al., 2006).

The NATO STO AVT-251 Task Group has developed better numerical tools to design a multifunctional unmanned combat air vehicle (Van Rooij & Cummings, 2018). The Aerodynamic group is conducting a performance study on design optimisation that enhances lift by utilising induced vortices and is attempting to exercise some control over the intensity and location of vortices to meet the flying performance, stability, and control requirements (Schütte et al., 2018). They carried out comprehensive parametric investigations aimed at discerning how the core geometric attributes impact the formation of the vortex and its associated aerodynamic characteristics. Achieving adequate yaw control is challenging due to the tailless nature of the design (Cummings et al., 2018).

As part of the Technical Cooperation Programme (TTCP) partners' collaborative CFD code validation exercise, (Petterson, 2006) conducted computational research into a typical UCAV design's low-speed aerodynamic and fluid properties. This research presents preliminary findings, including a comparison of the influence of the turbulence model on global coefficients, as well as the patterns of the flow field, to the experiment. This study helps to alter the profile of the wings' leading edge (Sukruthi et al., 2021). The leading edge of the standard configuration should be spherically blunt. NATO STO Task Group AVT-25 has been redesigning an effective, agile UCAV to suit specific mission criteria. The workgroup is a continuation of earlier groups that investigated the SAC-CON UCAV shape using a wind tunnel and CFD simulations and control surface effectiveness estimates. The redesign produced a new geometry known as MULDICON (Aelaei et al., 2019). The researchers employed Computational Fluid Dynamics (CFD) simulations to generate the aerodynamic data, which involves a comparative analysis of low-cost and low-fidelity Euler simulations with high-cost but high-fidelity RANS simulations in the context of Computational Fluid Dynamics simulation (Zimper & Hummel, 2018; Peng et al., 2023).

This study aims to determine the ideal back sweep angle for the lambda wing design to achieve the highest possible lift coefficient (C_L), the lowest possible drag coefficient (C_D), and the highest possible lift-to-drag ratio. The study is conducted at a low subsonic speed at different angles of attack, which is ideal for UCAV operation. The design aims to produce a high-lift UCAV with less drag. This design also gives high structural stability for a given wing shape.

2. NUMERICAL AND EXPERIMENTAL ANALYSIS

The scaled model (1:50) is 3D printed in PLA (Polylactic Acid). The project utilises the 3D printed Model as its baseline. Six models were fabricated, each characterized by different back sweep angles (δ = 0°, 10°, 20°, 30°, 40°, and 50°), as shown in Fig. 2 and detailed in Tables 1 and 2.

A Low-speed Wind Tunnel tests the Model at different freestream conditions. The tunnel operates on the principle of subsonic suction and is equipped with a test section measuring 600mm by 600mm by 1800mm

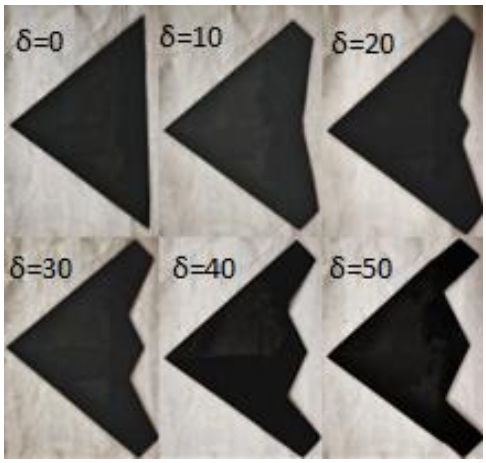

Fig. 2 Wing models at different back sweep back angle

Table 1 Back sweep angle and span area

Back sweep angle (δ)	Span area (m^2)
$\delta = 0^0$	0.039
$\delta = 10^0$	0.038
$\delta = 20^0$	0.036
$\delta = 30^0$	0.034
$\delta = 40^0$	0.0331
$\delta = 50^0$	0.032

Table 2 Wing Configuration Data

NACA series	(NACA 64A-010)
Root chord	20.61 cm
Wing span	30.8 cm
Tip chord	4.4 cm
Axis length	21.6cm
Mean aerodynamic chord	0.1496602317 m

(length). The tunnel's capabilities include achieving air speeds of up to 50m/s, ensuring a comprehensive range for experimentation with a contraction ratio of 9:1, the tunnel optimizes the airflow for accurate and controlled testing conditions. The overall dimensions of the wind tunnel measure 1.2m by 2.2m by 7.0m, providing a spacious and versatile environment for experimental setups. The tunnel is equipped with a drive system featuring an axial flow fan driven by a variable-speed DC motor, controlled by a thyristor controller. This configuration allows for precise adjustments in wind speed to accommodate a range of experimental scenarios. The inclusion of a six-component balancing system with a digital indicator enhances the accuracy and stability of the testing environment.

A six-component balance system installed in the tunnel collects forces and momentum acting on the Model at other conditions. The baseline configuration and modified back sweep angle configurations are positioned simultaneously in the test section at different angles of attack and free stream velocities. The further end of the mounting platform of the model is fastened to the six-component balance just beneath the test section. The locking screw mechanism in the mount allows for adjusting the model's angles of attack. (Fig. 3).

Different configurations were evaluated in a low-speed, open-type subsonic wind tunnel at varied attack

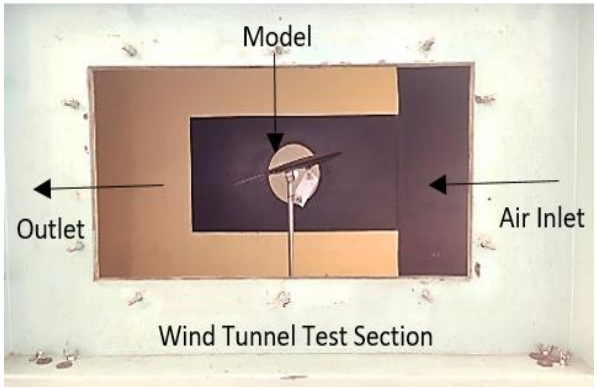

Fig. 3 Wing mounted at the center of wind tunnel test section

angles of $\alpha = -10^0, -5^0, 0^0, 5^0, 10^0$, and 15^0 with free stream velocities of V_∞ = 5, 10, 15, 20 m/s. The lift coefficient (C_L) is calculated from the provided lift values using the lift-force formula that derives lift as the product of pressure distribution around the body and the body's exposed surface area (S).

The following formula calculates the C_L value for the wing reference area, the air density value at sea level and free stream velocity at the test section.

$$L = \frac{1}{2} C_L \rho V_\infty^2 S \quad (1)$$

$$D = \frac{1}{2} C_D \rho V_\infty^2 S \quad (2)$$

$$Re = \frac{\rho V_\infty C}{\mu} \quad (3)$$

Similar to the measurement of the lift coefficient, the measurement of the drag force acting on the model uses the strain indicator of the six-component balance and determines the wing's drag coefficient (C_D).

Reynolds number is the ratio of inertia to viscous force. The mean Aerodynamic Chord (c) of the wing is used as the model length for calculating the Reynolds number (Re), while viscosity (μ) and density (ρ) are assumed to be at sea level.

The Lambda wing, characterized by a 40^0 sweep angle, was designed using the CATIA V5 program and simulated using the ANSYS Fluent software. The simulation utilises a solution based on pressure and integrates the SST k-ω turbulence model to represent the impacts of boundary layer interactions effectively.

The SST k-ω model integrates a rotating tensor and blending function to adjust turbulent viscosity, preserving similarity to the conventional k-ω model. Moreover, it introduces a blending function and integrates a cross-diffusion term into the ω equation, ensuring appropriate behavior of the model equations both in regions distant from the source and in proximity to the walls. The determination of specific dissipation rate (ω) and turbulence kinetic energy (k) is achieved through subsequent transport equations.

For k:

$$\frac{\partial}{\partial t}(\rho k) + \frac{\partial}{\partial x_i}(\rho k u_i) = \frac{\partial}{\partial x_j}\left[\Gamma_k \frac{\partial k}{\partial x_j}\right] + G_k - Y_k + S_k \quad (4)$$

For ω:

$$\frac{\partial}{\partial t}(\rho \omega) + \frac{\partial}{\partial x_i}(\rho \omega u_i) = \frac{\partial}{\partial x_j}\left[\Gamma_\omega \frac{\partial \omega}{\partial x_j}\right] + G\omega - Y_\omega + D_\omega + S_\omega \quad (5)$$

The wing is designed using CATIA V5, a parametric-based computer-aided design (CAD) software known for its capability to create detailed models with high precision and minimum room for mistakes. The domain is rectangular in shape, featuring a velocity inlet and pressure outlet, with non-slip wall conditions applied. The blockage ratio is set at 1.25.

The wing surfaces were discretized with approximately 25 Lakh nodes. In the viscous grid, the first layer's height was set at 4e-6 m, ensuring a y+<1 value less

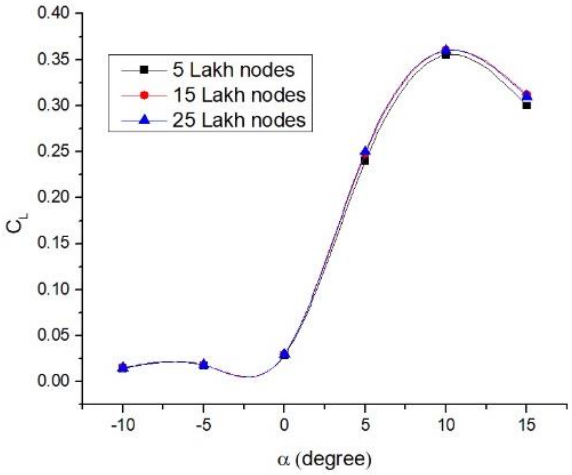

Fig. 4 Grid independence for varying mesh size

than 1 over the wing surface. A comprehensive set of 40 prismatic layers was created, exhibiting a growth rate of 1.25. To ensure grid independence, a systematic study was conducted on the base model, where the mesh size was varied within the range of 5 to 25 lakh nodes. The decision to opt for 25 lakh nodes was made based on its close correlation with the findings derived from experimental results. (Fig. 4)

To investigate the characteristics throughout the body, a fluid domain with dimensions about five times the chord length of the double delta wing has been selected. Pressure contours are utilised to get a deeper understanding of the properties shown by the upper and lower surfaces of a fluid.

3. RESULTS AND DISCUSSION

The study has shown a positive correlation between sweep back angle and efficiency. More precisely, the results suggest that, as the sweep back angle increases, there is a corresponding improvement in efficiency. The results demonstrate a decrease in the drag coefficient as the Reynolds number increases, corresponding to the shift from laminar to turbulent flow. This observation suggests a significant correlation between the geometric arrangement of the back angle and the aerodynamic efficiency of the system. The following sections provide a thorough examination

The efficiency gains of roughly 5-10% for every 10^0 degrees of sweep-back angle are observed. Furthermore, the lift coefficient decreases progressively with increasing Reynolds number due to the gradual development of flow separation at the trailing edge. At $\delta=10^0$, vortices formed on the wing's upper surface, beginning at the leading edge. There are statistically significant peaks in the local lift distribution at these points. As the angle of attack increases, there is a corresponding increase in the vortices. At $\alpha = 10^0$, a vortex forms at the wingtips and migrates towards the trailing edge as the angle of attack increases the expansion and inward advancement of the local lift, reducing its intensity. The observed phenomenon matches the characteristics of vortex breakup. At 10° and higher angles of attack, the UCAV's aerodynamics become non-linear and unstable due to flow separation and heavy vortices.

Up to α=10° or C_L=1.74, there is no appreciable increase in the stall or vortex lifts, and the lift curve slopes are reasonably linear. It is also clear that the (40°) wing has more lift than the baseline wing at all angles between $\delta=0^0$ and $\delta=50^0$ degrees (Fig. 5-8). Most of the lift generated by the baseline wing is reduced at the localised level, resulting in a more noticeable impact. In the context of aerodynamics, focusing on the robust, leading-edge vortices forming at the highly swept lambda wing's front edge is imperative. Following the collapse of a vortex, the surface pressure along the wing experiences pronounced fluctuations due to the disordered nature of the core flow. When the angle of attack (α) is elevated, the orderly structure within the core flow of the leading-edge vortex is abruptly disrupted, a phenomenon commonly referred

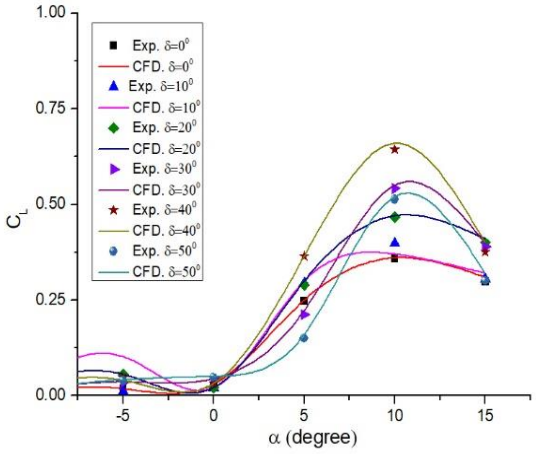

Fig. 5 Coefficient of Lift (C_L) vs. Angle of Attack (α) for different Back sweep angle (δ) at Reynold's Number = 50644

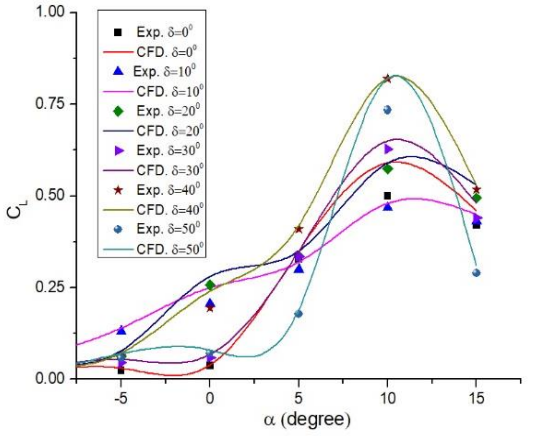

Fig. 6 Coefficient of Lift (C_L) vs. Angle of Attack (α) for different Back sweep angle (δ) at Reynold's Number=101289

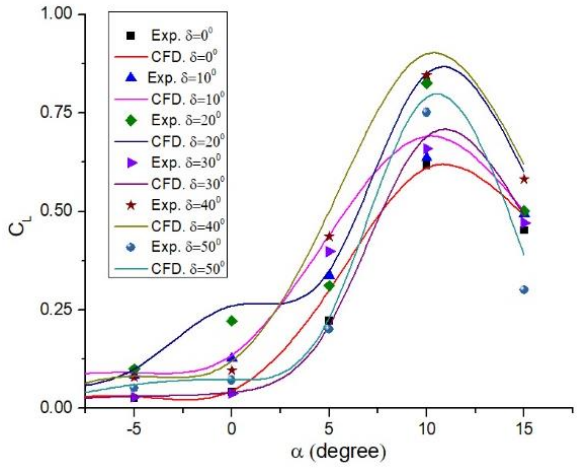

Fig. 7 Coefficient of Lift (C_L) vs. Angle of Attack (α) for different Back sweep angle (δ) at Reynold's Number=151934

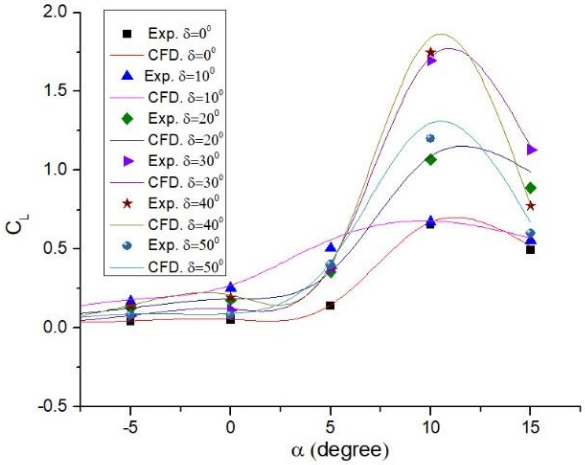

Fig. 8 Coefficient of Lift (C_L) vs. Angle of Attack (α) for different Back sweep angle (δ) at Reynold's Number=202579

to as vortex breakdown. When the wing is set at a sweep-back angle of 10°, a small vortex forms at the tip of the wing. This vortex moves towards the center of the wing and becomes larger as the angle of attack increases. Nevertheless, the decrease in the windward wing's effective sweep reduces the lifting capacity of the vortex, leading to a loss of lift near the wingtips where flow separation occurs. Increasing the effective sweep angle on the wing located on the side opposite to the wind direction helps to improve the ability of the vortex to generate lift.. The reduction in local lift occurs as the vortex undergoes a weakening process and shifts towards the tail region due to expansion. An analysis of the vortex might explain this phenomenon. The aerodynamics of an Unmanned Combat Aerial Vehicle (UCAV) exhibit non-linear behaviour and instability when subjected to angles of attack above 15^0 degrees. This phenomenon arises primarily due to flow separations, and the formation of vortices was observed to not have significant flow characteristics for the angle of attack is below $\alpha = 0^0$. A vortex is generated at an angle of $\alpha = 10^0$ on the baseline, exhibiting downstream movement from the wingtip (Fig. 9-12). Furthermore, it is possible to observe a secondary, small vortex near the wingtip. The wingtip separation exhibits a greater extent and diffusion, resembling a bubble-like separation, but the top vortex maintains a compact structure with a small radius, enhancing lift generation.

Pressure is crucial in generating the required lift for an Unmanned Combat Aerial Vehicle (UCAV). As the angle of attack is augmented, a concomitant increase in pressure on the lower surface and a decrease in pressure on the upper surface will occur. The flow will manifest a rotational movement from the lower to the upper surface due to the disparity in pressure, generating an upward force exerted on the object. The contour plots generated by Computational Fluid Dynamics (CFD) analysis provide valuable insights into the pressure distribution throughout the model's surface (Fig.13-16).

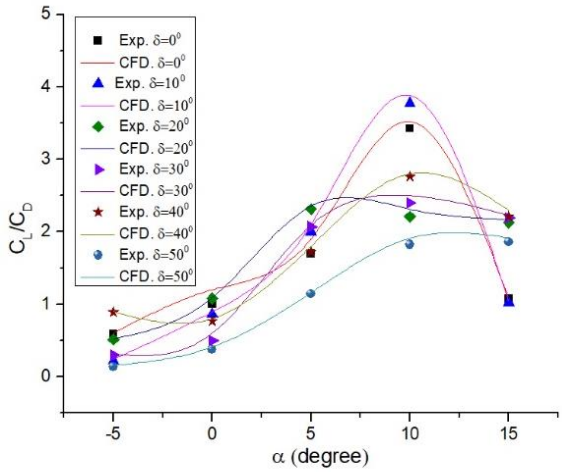

Fig. 9 Coefficient of Lift (C_L/C_D) vs. Angle of Attack (α) for different Back sweep angle (δ) at Reynold's Number=50644

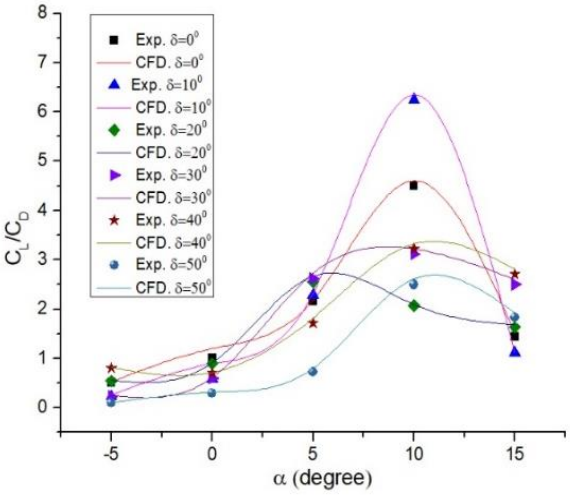

Fig. 10 Coefficient of Lift (C_L/C_D) vs. Angle of Attack (α) for different Back sweep angle (δ) at Reynold's Number=101289

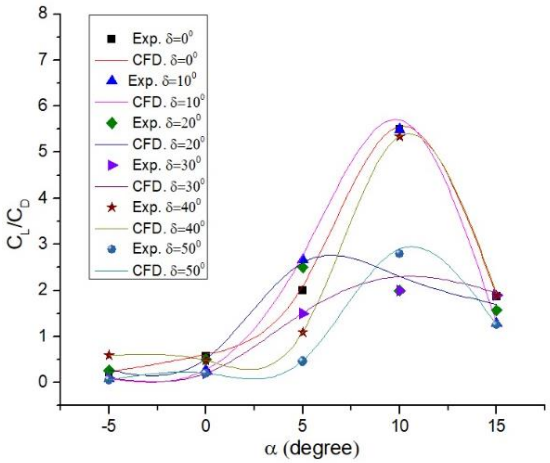

Fig. 11 Coefficient of Lift (C_L/C_D) vs. Angle of Attack (α) for different Back sweep angle (δ) at Reynold's Number=151934

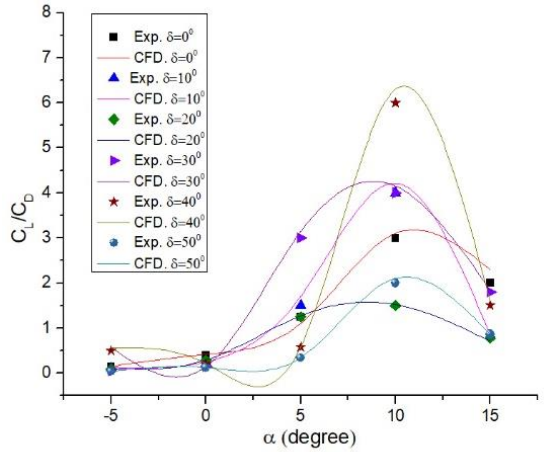

Fig. 12 Coefficient of Lift (C_L/C_D) vs. Angle of Attack (α) for different Back sweep angle (δ) at Reynold's Number=202579

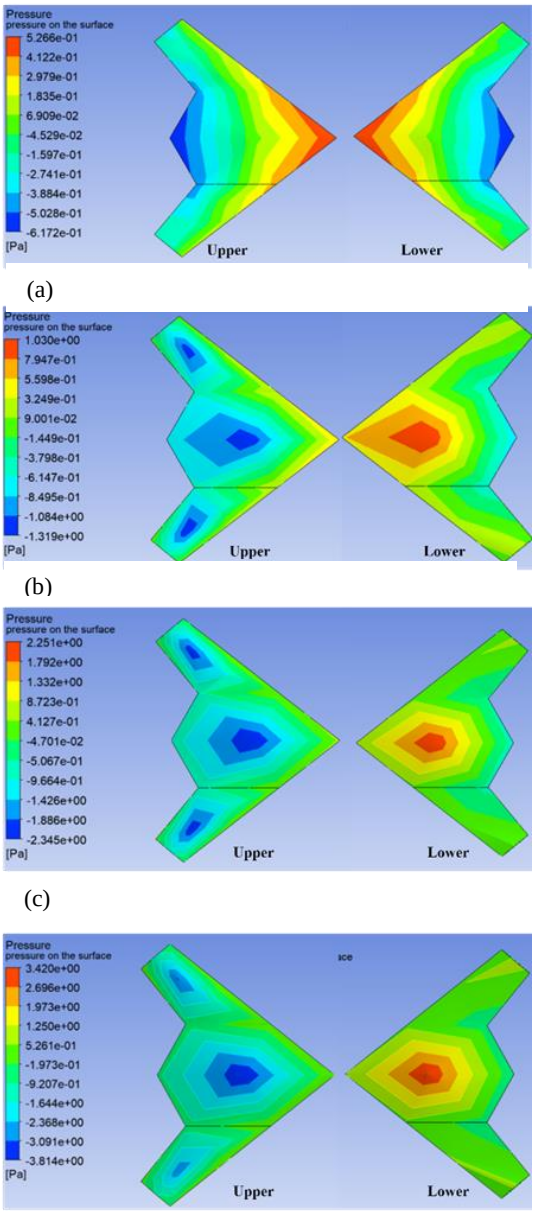

Fig. 13 Pressure Contour of Lambda Wing with 40° Back sweep angle (δ =40⁰) at Reynold's Number=50644 across Various Angles of Attack (a. α=0⁰, b. α=5⁰, c. α=10⁰, d. α=15⁰)

When the angle of attack is zero, the stagnation point at the apex of the model remains unchanged. However, as we increase the angle of attack from $\alpha=5^0$ to $\alpha=10^0$, we observe that the stagnation point moves from 25% to 35% along the chord towards the lower surface (pressure surface). At $\alpha=15^0$, there is a shift in the stagnation point position to 38% along the aerodynamic chord from the apex.

Comprehending the aerodynamic characteristics of airflow across a wing is crucial in aerodynamic design and performance evaluation. The location of the stagnation point and the nature of flow separation are crucial factors in defining the aerodynamic properties of a lambda wing. Furthermore, it has been shown that significant flow separation occurs near the Mean Aerodynamic Point (MAP) at different angles of attack, influencing alterations in the performance of the wing. It is important to note that flow separation is not found at the Mean Aerodynamic Point when the $\alpha = 0^0$, which emphasises the significant influence of the angle of attack on flow separation events. At elevated angles of attack, $\alpha = 15^0$, tail flow separation is mitigated due to decreased flow along the chord-wise direction and an augmentation in flow along the span-wise direction. The modification in flow characteristics is a noteworthy determinant impacting stall behaviour. (Fig. 17).

The circulation control efficiency was diminished by the strong vortex flow observed at high angles of attack. The change in vortex flow and lift production of a lambda wing with a 50° sweep angle as one moves from the wing's upper surface to its tip. The rise in lift within the range of moderate-to-high angles of attack was attributed to a collapsed apex, leading to a delay stall. By

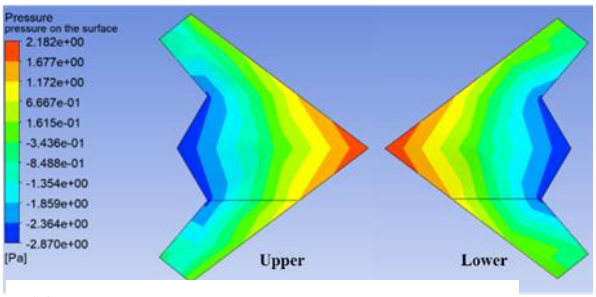

(a)

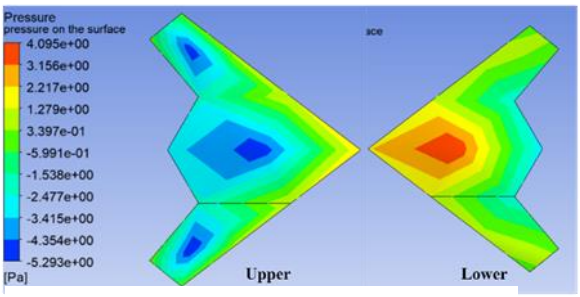

(b)

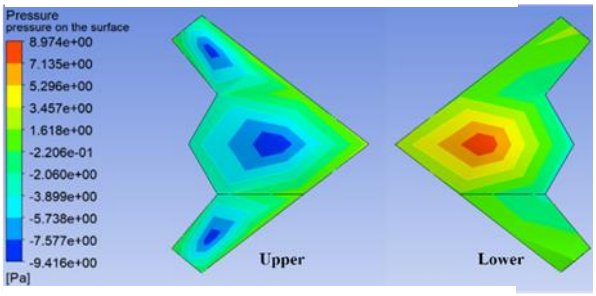

(c)

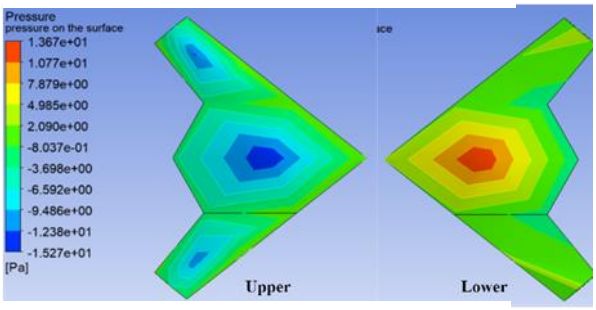

(d)

Fig. 14 Pressure Contour of Lambda Wing with 40° Back sweep angle (δ =40^0) at Reynold's Number=101289. across Various Angles of Attack (a. α=0^0, b. α=5^0, c. α=10^0, d. α=15^0)

making adjustments to both the joint top and the tip flap, the lift was increased and the reduction of the leading-edge vortex was slowed down, resulting in deceleration. The use of the upper flap and the tip flap led to the shifting of the Vortex at the leading edge away from the centreline and its repositioning closer to the wing's upper surface.

When the Reynolds number values are low, the flow transitions into a region called creeping flow or Stokes flow, leading to a decrease in the drag coefficient. The generation of lift results from an imbalance in pressure, yet this phenomenon gives rise to challenges at the wingtips. During the flight, the wing generates a pressure differential, causing air with high pressure underneath it to ascend over the wing's tip and into the lower-pressure region above.

The forward movement generated by the wings induces an upward air outflow, forming a lengthy circular pattern resembling a vortex. This phenomenon, sometimes called vortex drag, is observed as it decreases from the wing tip. The occurrence of vortices throughout the whole trailing edge of the wing leads to a decrease in air pressure, resulting in an escalation of pressure drag.

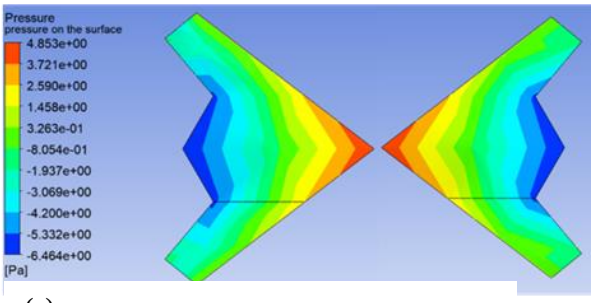

(a)

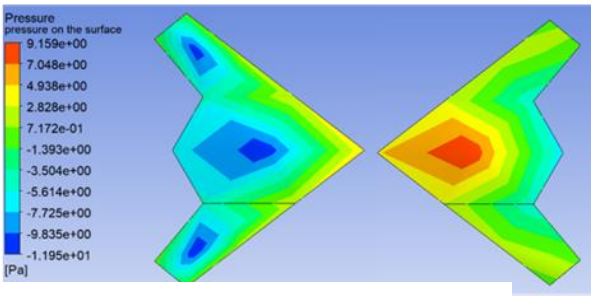

(b)

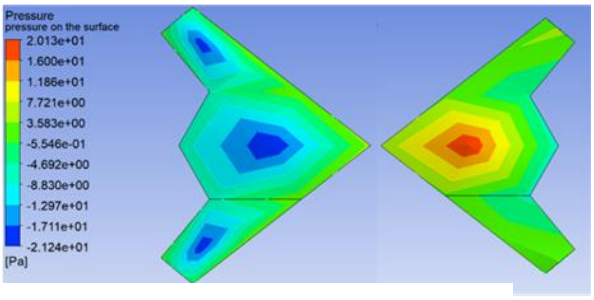

(c)

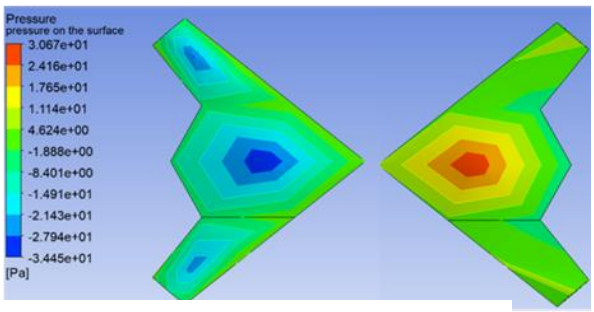

(d)

Fig. 15 Pressure Contour of Lambda Wing with 40° Back sweep angle (δ =40^0) at Reynold's Number=151934. across Various Angles of Attack (a. α=0^0, b. α=5^0, c. α=10^0, d. α=15^0)

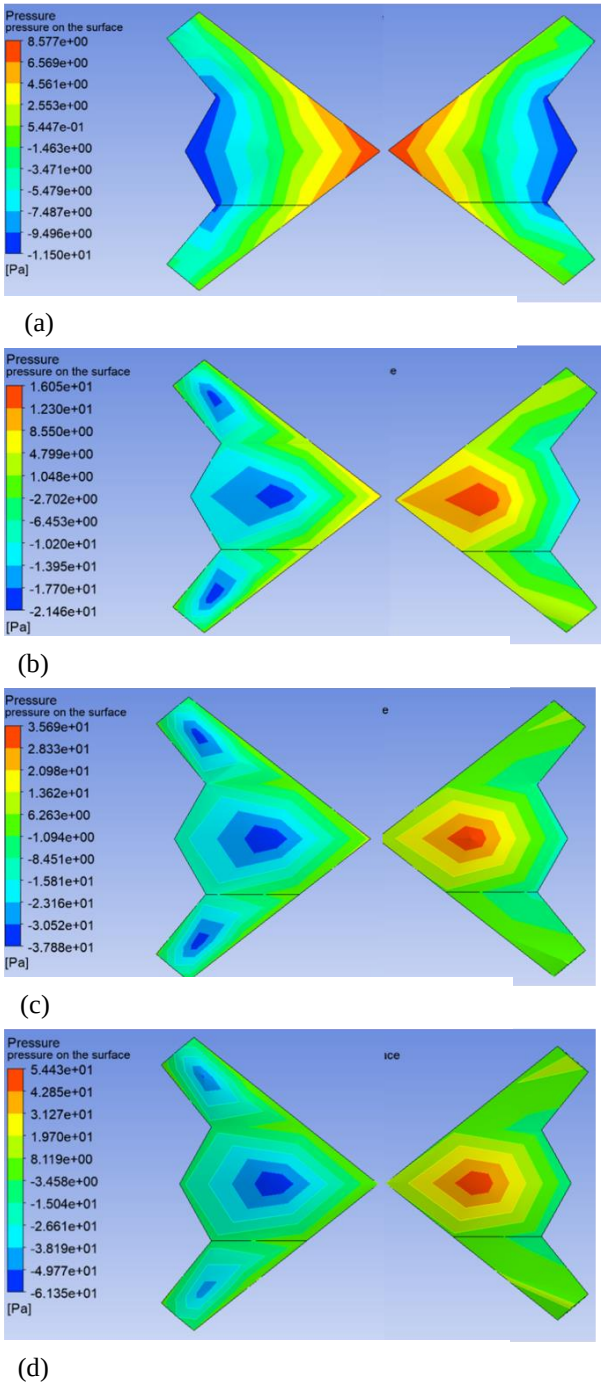

Fig. 16 Pressure Contour of Lambda Wing with 40° Back sweep angle (δ =40^0) at Reynold's Number=202579. across Various Angles of Attack (a. α=0^0, b. α=5^0, c. α=10^0, d. α=15^0)

4. CONCLUSION

This study demonstrates a negative correlation between the values of C_L and C_D and the Reynolds number. The drop in these values may be related to the development and strengthening of tip vortices, which become more prominent as the back angle increases. The most significant value of tip vortices was observed at a back sweep angle 40^0. A rearward sweep angle of 40^0 degrees is advisable to achieve an optimal balance

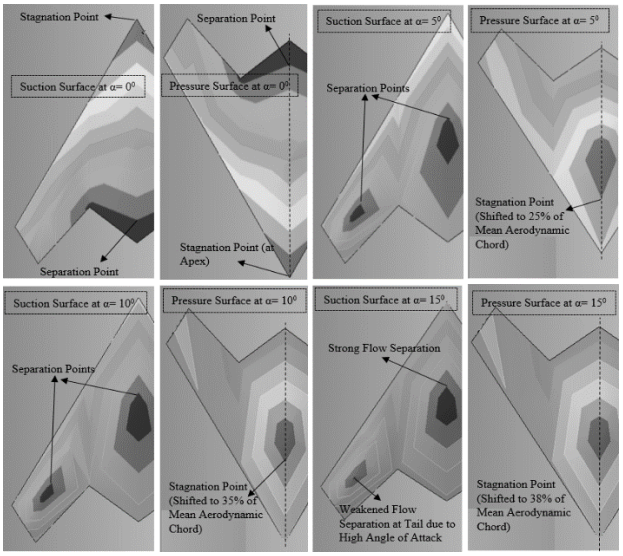

Fig. 17 Locations of Flow Separation on Wing at Various Angles of Attack (δ=40°)

between lift and drag. The observed value of the minimum coefficient of drag is 0.1911 at an angle of attack of 10^0. This implies that it produces a higher lift and a reduced drag than the base delta design. In conclusion, the investigation into varying sweep-back angles has revealed notable efficiency gains, ranging approximately from 5% to 10% for every 10^0 degrees of sweep-back. Furthermore, our findings indicate that at a zero angle of attack, the stagnation point at the apex of the model remains constant. However, as we increase the angle of attack from α = 5^0 to α = 10^0, a distinct shift in the stagnation point is observed, moving from 25% to 35% along the chord towards the lower surface.

ACKNOWLEDGEMENTS

The authors would like to express their gratitude to the National Mission – Interdisciplinary Cyber-Physical Systems (NM-ICPS), TiHAN, Indian Institute of Technology (IIT) Hyderabad for providing facilities for the conduct of this research.

CONFLICT OF INTEREST

I declare that there are no conflicts of interest to disclose.

AUTHORS CONTRIBUTION

All three authors have made significant contributions towards Experimental Investigation, Research Methodology, Data curation, Formal Analysis, Writing – Original Draft Preparation and critical revision of the article.

REFERENCES

Aelaei, M., Karimian, S., & Ommi, F. (2019). Sensitivity analysis and optimization of delta wing design parameters using CFD-Based response surface

method. *Journal of Applied Fluid Mechanics*, *12*(6), 1885–1903. https://doi.org/10.29252/jafm.12.06.29706

Al-Garni, A. Z., Saeed, F., & Al-Garni, A. M. (2008). Experimental and numerical investigation of 65 degree delta and 65/40 degree double-delta wings. *Journal of Aircraft*, *45*(1), 71–76. https://doi.org/10.2514/1.20243

Chaplin, R., & Birch, T. (2012, June 25). *The aero-acoustic environment within the weapons bay of a generic UCAV*. 30th AIAA Applied Aerodynamics Conference. https://doi.org/10.2514/6.2012-3338

Coppin, J., Birch, T., Kennett, D., Hoholis, G., & Badcock, K. (2018). Prediction of control effectiveness for a highly swept unmanned air vehicle configuration. *Journal of Aircraft*, *55*(2), 534–548. https://doi.org/10.2514/1.c033988

Cummings, R. M., & Schütte, A. (2012). Integrated computational/experimental approach to unmanned combat air vehicle stability and control estimation. *Journal of Aircraft*, *49*(6), 1542–1557. https://doi.org/10.2514/1.c031430

Cummings, R. M., Liersch, C., & Schuette, A. (2018). *Multi-Disciplinary design and performance assessment of effective, agile NATO air vehicles*. 2018 Applied Aerodynamics Conference. https://doi.org/10.2514/6.2018-2838

Frink, N. T., Tormalm, M., & Schmidt, S. (2012). Three unstructured computational fluid dynamics studies on generic unmanned combat aerial vehicle. *Journal of Aircraft*, *49*(6), 1619–1637. https://doi.org/10.2514/1.c031383

Lakshmanan, D., Boopathi, R., & Saravanan, P. (2023). Aerodynamic investigation and simulation studies on wing section of an unmanned aerial vehicle attached with solar plate. *Journal of Applied Fluid Mechanics*, *16*(8), 1666-1674. https://doi.org/10.47176/jafm.16.08.1680

Nagel, A., Levy, D. E., & Shepshelovich, M. (2006, January 9). *Conceptual aerodynamic evaluation of Mini/Micro uav*. 44th AIAA Aerospace Sciences Meeting and Exhibit. https://doi.org/10.2514/6.2006-1261

Peng, X., Kou, J., & Zhang, W. (2023). Multi-fidelity nonlinear unsteady aerodynamic modeling and uncertainty estimation based on Hierarchical Kriging. *Applied Mathematical Modelling*, *122*, 1–21. https://doi.org/10.1016/j.apm.2023.05.031

Petterson, K. (2006, January 9). *CFD Analysis of the Low-Speed Aerodynamic Characteristics of a UCAV*. 44th AIAA Aerospace Sciences Meeting and Exhibit. https://doi.org/10.2514/6.2006-1259

Schütte, A., Huber, K. C., Frink, N. T., & Boelens, O. J. (2018, March). Stability and control investigations of generic 53 degree swept wing with control surfaces. *Journal of Aircraft*, *55*(2), 502–533. https://doi.org/10.2514/1.c033700

Sukruthi, C., Ashika, & Shali, S. (2021). *Analysis of subsonic flow over delta winged aircraft.* Seventh International Symposium on Negative Ions, Beams and Sources (Nibs 2020). https://doi.org/10.1063/5.0057922

Syam Narayanan, S., & Asad Ahmed, R. (2021). Effect of fluid-structure interaction on noise generation in MAV with fixed and flapping membrane wing. *Journal of Applied Fluid Mechanics*, *14*(6), 1817-1826. https://doi.org/10.47176/jafm.14.06.32855

Syam Narayanan, S., & Asad Ahmed R. (2022). Effect of chord-wise flexibility in the lift generation of flapping MAV with membrane wing. *Aircraft Engineering and Aerospace Technology*, *94*(5), 792–798. https://doi.org/10.1108/aeat-03-2021-0070

Van Rooij, M., & Cummings, R. M. (2018, June 24). *Aerodynamic design of an unmanned combat air vehicle in a collaborative framework*. 2018 Applied Aerodynamics Conference. https://doi.org/10.2514/6.2018-2840

Younis, Y., Bibi, A., Haque, A. U., & Khushnood, S. (2012). Vortical flow topology on windward and leeward side of delta wing at supersonic speed. *Journal of Applied Fluid Mechanics*, *2*(2), 13-21. https://doi.org/10.36884/jafm.2.02.11860

Zimper, D., & Hummel, D. (2018). Analysis of the transonic flow around a unmanned combat aerial vehicle configuration. *Journal of Aircraft*, *55*(2), 571–586. https://doi.org/10.2514/1.c033697